Energy Storage Materials 39 (2021) 176–185

Contents lists available at ScienceDirect

Energy Storage Materials

journal homepage: www.elsevier.com/locate/ensm

Optimal electrode-scale design of Li-ion electrodes: A general correlation

Zeyu Hui [a,b], Karthik S. Mayilvahanan [a], Krystian Ganko [a], Yuan Yang [b], Xiao Zhang [c], Zhengyu Ju [c], Kenneth J. Takeuchi [d,e,f], Amy C. Marschilok [d,e,f,g], Guihua Yu [c], Esther Takeuchi [d,e,f,g], Alan C. West [a,h,*]

[a] Department of Chemical Engineering, Columbia University, New York, New York 10027, USA
[b] Department of Applied Physics and Applied Mathematics, Columbia University, New York, New York 10027, USA
[c] Materials Science and Engineering Program and Department of Mechanical Engineering, The University of Texas at Austin, Austin, Texas 78712, USA
[d] Institute for Electrochemically Stored Energy, Stony Brook University, Stony Brook, New York 11794, USA
[e] Department of Chemistry, Stony Brook University, Stony Brook, New York 11794, USA
[f] Department of Materials Science and Chemical Engineering, Stony Brook University, Stony Brook, New York 11794, USA
[g] Interdisciplinary Science Department, Brookhaven National Laboratory, Upton, NY 11973, USA
[h] Department of Earth and Environmental Engineering, Columbia University, New York, New York 10027, USA

ARTICLE INFO

Keywords:
Li-ion battery
Volumetric energy density
Electrode design
General correlation

ABSTRACT

Multi-scale physics-based models, which have been parameterized and validated with discharge experiments, are optimized by varying porosity and mass loading to achieve maximum energy density. Although transport losses occur on both the electrode and particle scales, the electrode-scale optimal design is independent of the smaller scale properties. Electrode-scale properties such as tortuosity, electrolyte concentration, and Li-ion diffusion coefficient all impact optimal design. However, the impact can be generalized and the optimal results follow a general design rule that is captured in convenient correlations: $\epsilon = 0.13\ \log_{10}(\ k_\epsilon \frac{C_r \tau}{F D_0 c_0})$ and $Q_a = k_Q / \sqrt{k_\epsilon C_r \tau/(F D_0 c_0)}$, which provide guidelines for optimization of electrode architectures. The correlations are also in agreement with prior optimization results in the literature.

1. Introduction

Energy storage is a key technology to enable widespread adoption of intermittent, renewable energy sources [1–3]. Lithium ion batteries (LIBs) are widely used because they are characterized by high energy density, high power density, and good cycle life [4]. Nevertheless, new applications often place new requirements on LIBs. Broad application of LIBs on the electric vehicle (EV) market requires the current batteries to have higher energy density, in order to cut cost and prolong mileage [5,6]. Improvements can be achieved by new intercalation materials [7–9] as well as by optimizing cell design.

Among the different factors that limit the improvement of battery energy density, transport impedances are crucial [10,11]. As a complex system, ion transport impedances may arise on different length scales inside the porous battery electrode [12]. For example, as depicted in Fig. 1, transport of lithium ions may take place on multiple length scales inside the $Li_xNi_{1/3}Mn_{1/3}Co_{1/3}O_2$ (NMC_{111}) electrode. During battery operation, lithium ions inside the liquid electrolyte not only diffuse through the porous electrode (electrode scale), but also diffuse through secondary agglomerates formed by crystals (agglomerate scale). Meanwhile, intercalated lithium must also diffuse from the crystal surface to its center (crystal scale). It may be difficult to determine whether ion transport impedances are more important on the agglomerate or crystal scale [13]. It may be however more straightforward to design electrodes where electrode-scale ion transport impedance is minimal, and this can be an important strategy in laboratory investigations of agglomerate and crystal scale transport [14,15], also a widely adopted method to increase cell energy density.

Newman and collaborators reported the application of a physics-based model on cell energy density optimization and design [16,17]. Fuller *et al.* [16] constructed the dual-insertion model and simulated the performance of the graphite/$LiMn_2O_4$ cell, optimizing the specific energy and specific power of such cell by varying cathode thickness and porosity. However, only one parameter was changed at a time in this study. Srinivasan *et al.* [18] used a model to perform simultaneous optimization of anode and cathode thicknesses and porosities to improve energy density of graphite/$LiFePO_4$ cells. Appiah *et al.* [19] applied a similar approach to graphite/$LiNi_{0.6}Co_{0.2}Mn_{0.2}O_2$ cells, optimizing for

* Corresponding author:
E-mail addresses: zh2327@columbia.edu (Z. Hui), km3400@columbia.edu (K.S. Mayilvahanan), kkg2120@columbia.edu (K. Ganko), yy2664@columbia.edu (Y. Yang), xz6455@utexas.edu (X. Zhang), zyju@utexas.edu (Z. Ju), kenneth.takeuchi.1@stonybrook.edu (K.J. Takeuchi), amy.marschilok@stonybrook.edu (A.C. Marschilok), ghyu@austin.utexas.edu (G. Yu), esther.takeuchi@stonybrook.edu (E. Takeuchi), acw7@columbia.edu (A.C. West).

https://doi.org/10.1016/j.ensm.2021.04.018
Received 25 January 2021; Received in revised form 15 March 2021; Accepted 12 April 2021
Available online 20 April 2021

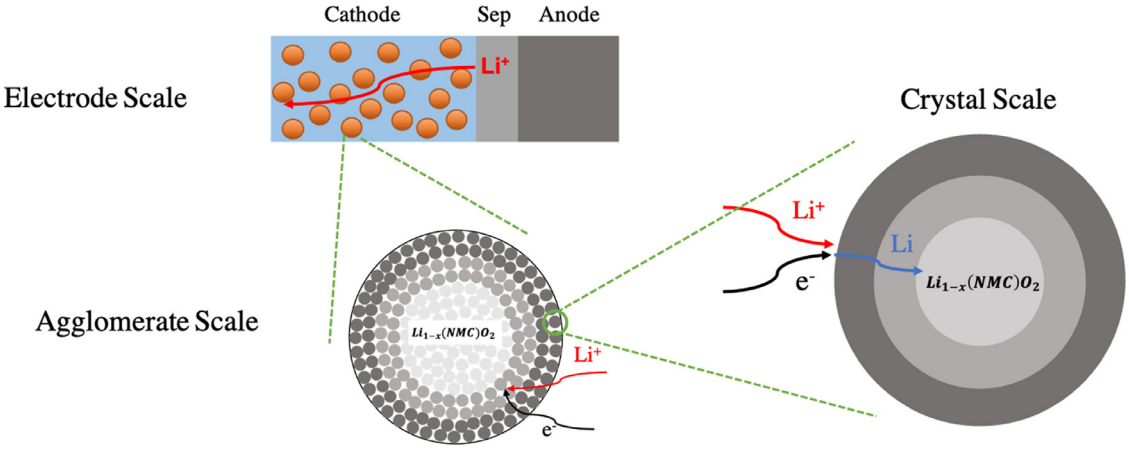

Fig. 1. Schematic illustration of lithium transport on different length scales of an NMC_{111} electrode. Most physics-based models couple the electrode scale with either an agglomerate or crystal scale description of transport processes.

List of Symbols

c_0	Concentration of lithium in the electrolyte [mol cm^{-3}]
C_r	Current rate, 1/time need to fully charge/discharge the cell [h^{-1}]
D_0	Diffusion coefficient for lithium ions in bulk electrolyte, 1×10^{-6} [cm^2 s^{-1}].
D_{agg}	Diffusion coefficient for lithium ions in secondary agglomerates [cm^2 s^{-1}].
E_V	Volumetric energy density [Wh L^{-1}]
E_A	Areal energy density [Wh cm^{-2}]
F	Faraday's constant, 96485 [C mol^{-1}]
$i_{applied}$	Applied current density [A cm^{-2}]
k_ϵ	Constant in general correlation expression, 11.94 [C cm^{-1}]
k_Q	Constant in general correlation expression, 38.03 [mAh cm^{-2}]
L_{anode}	Thickness of anode [μm]
L_{agg}	Agglomerate size [μm]
$L_{separator}$	Thickness of separator, 25 [μm]
$L_{cc}^{cathode}$	Thickness of cathode current collector [μm]
L_{cc}^{anode}	Thickness of anode current collector [μm]
L_{BOC}	Total thickness of inert components (balance of cell), 50 [μm]
M_A	Active material mass loading of electrodes [mg cm^{-2}]
Q_a	Capacity loading of electrodes [mAh cm^{-2}]
$Q_{cathode}$	Theoretical capacity of cathode material [mAh g^{-1}]
Q_{anode}	Theoretical capacity of anode material [mAh g^{-1}]
t_{dchg}	Discharge time [h]
V(t)	Cell Voltage as a function of time [V]
V_{AM}	Volume fraction of active material in terms of total electrode volume
V_{inert}	Volume fraction of inert additives (binder & conductor) in terms of total electrode volume
ϵ	Void fraction of porous electrode (porosity)
ϵ_{anode}	Porosity of graphite anode, 0.35
ρ_{AM}	Density of cathode active material [g cm^{-3}]
$\rho_{graphite}$	Density of graphite, 2.2 [g cm^{-3}]
σ	Electronic Conductivity [S cm^{-1}]
τ	Tortuosity of electrode
τ_{agg}	Characteristic time for agglomerate scale diffusion of lithium ion [s]

cathode porosity and thickness. De *et al.* [20] extended such algorithm to simultaneous optimization of different numbers of parameters, including porosities and thicknesses for cathode and anode. All of the previous studies focused on optimizing the electrode design of a specific type of active material.

In this study, we construct physics-based models validated against real experimental observations and use such experimental-validated models to optimize electrode-scale design parameters and show that agglomerate and crystal scale transport properties do not significantly affect the values of the electrode-scale design parameters needed to optimize energy density. We show with a re-scaling of the current rate, the optimal design parameters follow a general design rule, captured in convenient correlations. The cycling stability is not considered in the current study but would be important to optimize if degradation mechanisms can be captured in future models.

2. Theory and Methods

Physics-based models, validated by comparison with experimental discharge voltage profiles, are used to determine the optimal cathode design through sampling approaches that leverage high performance computer resources [21]. The physics-based continuum model used in this study followed the development by Newman et al., [22] but uses a finite-volume numerical method that allows for a more general treatment of the smaller scale, including phase change reactions as well as agglomerate and crystal-scale models. A detailed description of the NMC cathode model is given in the study by Hui et al. [13] A so-called pseudo 2D (P2D) modeling paradigm [23] was used to connect the smaller-length scale simulations to the parameters that are controlled during fabrication on the electrode scale. Equations describing transport of lithium inside the agglomerate or crystal are coupled to the electrode scale equations.

For thick electrodes relevant to high energy density applications [24], the performance of electrodes is strongly dependent on electrode-scale transport processes. To minimize the electrode scale transport loss and get highest energy density, the electrode porosity and active material loading were optimized by sampling in two-dimensional space. The tortuosity of the electrode is the major source of uncertainty in optimization, as it is difficult to measure directly but can have significant impacts on electrode-scale ion transport. Applicability of the proposed approach when considering this uncertainty in tortuosity is discussed.

As shown in Fig. 2a, to maximize the volumetric energy density (E_V) of a cell at a given current, there are two competing directions to be

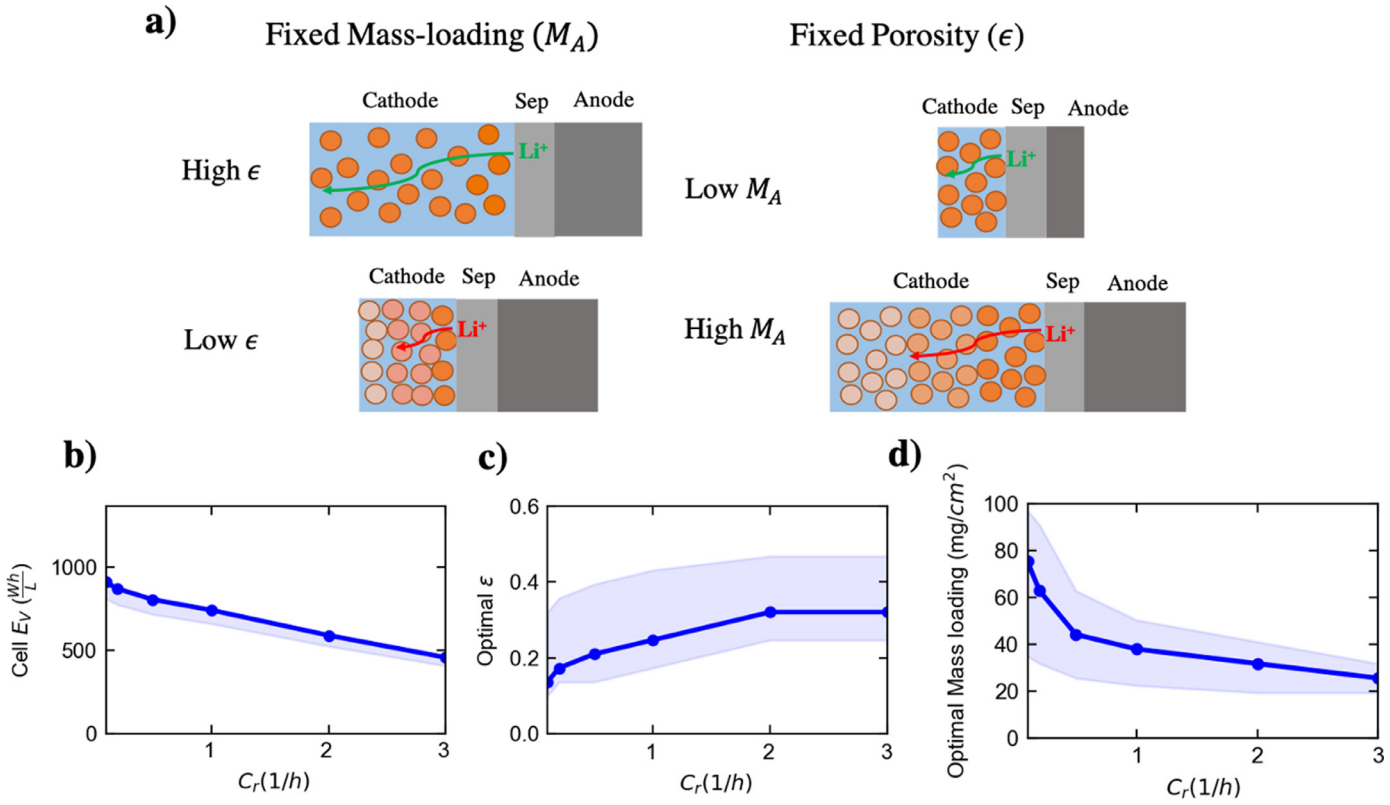

Fig. 2. (a) Schematic illustrating the key design parameters, mass loading and porosity. The thickness of the electrode is determined by these variables. (b) Optimal volumetric energy densities (E_V) over a range of discharge rates from C/10 to 3C (1C = 150 mA g^{-1}). (c,d) The optimal porosity and mass loading with which electrodes can be fabricated to achieve that optimal E_V. The shading shows the parameter value regions to reach 90 % of maximum E_V.

considered. While increasing areal mass loading of active material or making the electrode denser (less porous) tends to increase volumetric energy of the cell by using the space more efficiently, it leads to sluggish ion transport into the electrode, which decreases the utilization of electrode material. On the contrary, using thin and porous electrodes helps the electrode retain full utilization, but given that the thickness of the current collectors and separator are fixed, such design leads to low E_V because a large portion of the volume is occupied by inert components. Consequently, finding the balance between improving electrode utilization and increasing mass loading (or reducing electrode porosity) becomes the key of optimizing cell E_V.

The electrode scale optimal design followed the algorithm from Mayilvahanan et al. [25] Taking $Li_xNi_{1/3}Mn_{1/3}Co_{1/3}O_2$ (NMC_{111}) electrode as an example, the optimal result is shown in Fig. 2b, c, d. In addition to active material, electrodes may be comprised of other solid materials to impart mechanical integrity (e.g., binder) and to impart electronic conductivity (e.g., 10 % in volume of super C_{65}). Since such materials do not store Li ions, the optimal volume fraction of the component should be minimized, at for example a volume fraction slightly exceeding the percolation threshold [26,27]. Here, it is assumed that $V_{AM}/(V_{AM}+V_{inert}) = 0.9$, and Fig. S4 in the Supplementary Information shows the results from relaxing the assumption. In all cases, while a finite electronic conductivity is considered, it is sufficiently large that electronic resistances are minimal. Thus, optimal design is dependent primarily on the electrode porosity ($\epsilon = 1 - V_{AM} - V_{inert}$) and electrode areal mass loading (M_A in mg cm^{-2})

Parameter sets obtained from a grid sampling among the 2D parameter space (ϵ and M_A) were fed to the model to simulate performance. The volumetric energy density E_V is given by

$$E_V = \frac{E_A}{L_{cathode} + L_{anode} + L_{BOC}} \tag{1}$$

where the energy per area E_A is given by

$$E_A = \int_0^{t_{dchg}} V(t) i_{applied}\, dt \tag{2}$$

The thickness of cathode ($L_{cathode}$) is calculated by

$$L_{cathode} = \frac{M_A}{\rho_{AM} V_{AM}} \tag{3}$$

in which V_{AM} is the volume ratio between active material and the whole electrode (including volume of pores). The graphite anode is assumed to be capacity matched at a 1:1 ratio with cathode, given by

$$L_{anode} = \frac{Q_{cathode} M_A}{Q_{anode}(1-\epsilon_{anode})\rho_{graphite}} \tag{4}$$

in which the graphite anode porosity (ϵ_{anode}) is assumed to be fixed at 0.35. It is further assumed that the thickness of Balance of Cell (inert components) L_{BOC} (assumed to be 50 μm) is given by the sum of separator and current collector thicknesses:

$$L_{BOC} = L_{separator} + L_{cc}^{anode} + L_{cc}^{cathode} \tag{5}$$

In the Supplemental Information Fig. S3, we show that assumptions regarding the anode have minimal or no impact on optimal cathode design, as long as a fixed n:p capacity ratio is assumed.

The optimal volumetric energy density E_V is shown in Fig. 2b as a function of the current, given as a current rate (C_r). The corresponding optimal mass loading and porosity are shown in Fig. 2c and d and follow expected trends. For example, if one wants to design an NMC_{111} electrode which operates at $C_r = 1$ h^{-1}, electrodes with porosity of 0.26 and mass loading of 38 mg cm^{-2} gives the highest E_V. Increasing porosity or reducing mass loading reduces cell E_V due to increased cell volume or increased inert component ratio, while further reducing porosity or

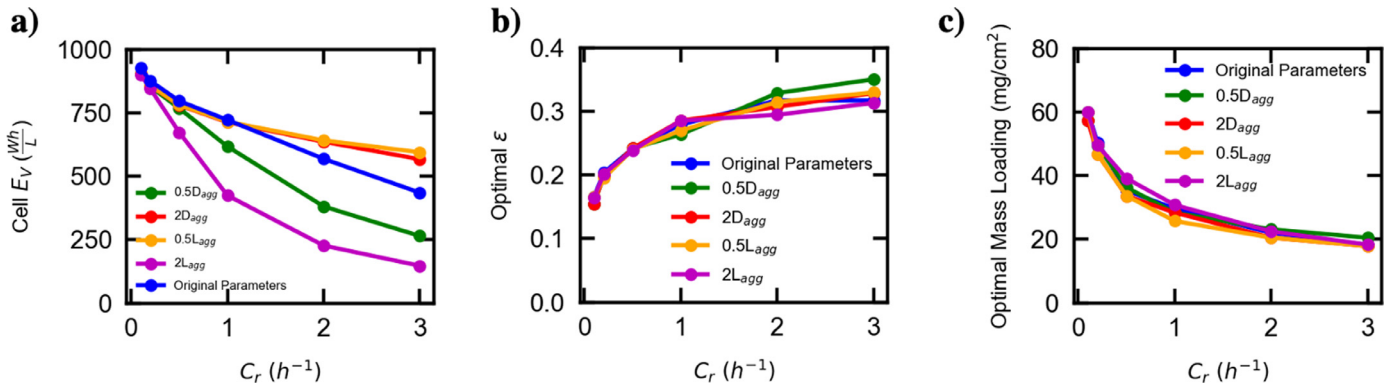

Fig. 3. (a) Optimal E_V obtained for different L_{agg} and D_{agg}. The original parameter refers to L_{agg} = 5 μm and D_{agg} = 1.4 × 10^{-9} cm^2 s^{-1}. (b,c) Optimal ε and M_A resulting from the assumed L_{agg} and D_{agg}.

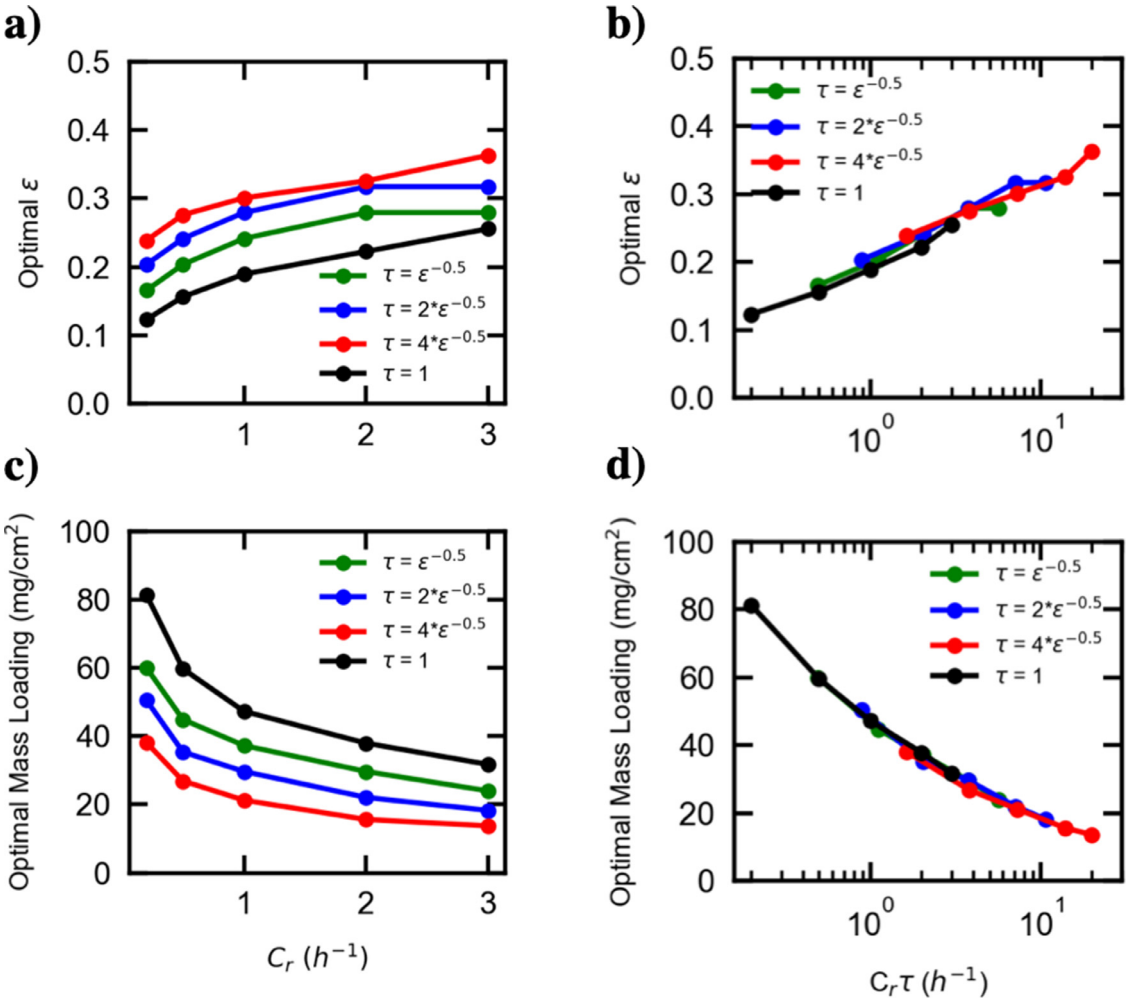

Fig. 4. Optimal electrode parameters depend strongly on the assumed tortuosity (a,c). However, if the C_r is multiplied by τ, the optimal ε and M_A follow a single curve (b,d).

increasing mass loading also reduces cell E_V due to reduction in material utilization (discharge capacity per gram of active material). The optimal ε increases while the optimal mass loading drops with increasing C_r, indicating that electrode should be more porous and also thinner to retain good utilization. The shaded regions provide an estimate of sensitivity of E_V to the design parameters, showing the range of values of one parameter that leads to 90% of the maximum achievable cell E_V when the other parameter is set at its optimal value. For example, if one synthesizes electrodes with mass loading of 38 mg cm^{-2}, any porosity in the range of 0.17-0.43 will yield an E_V that is within 90% of the optimum at C_r = 1C.

3. Results

3.1. Optimal cell E_v affected by smaller scale parameters

Battery performance is impacted by the ion transport impedances on both the electrode scale and the smaller scales. Previous work [13] has shown that the agglomerate scale may be the dominant smaller length

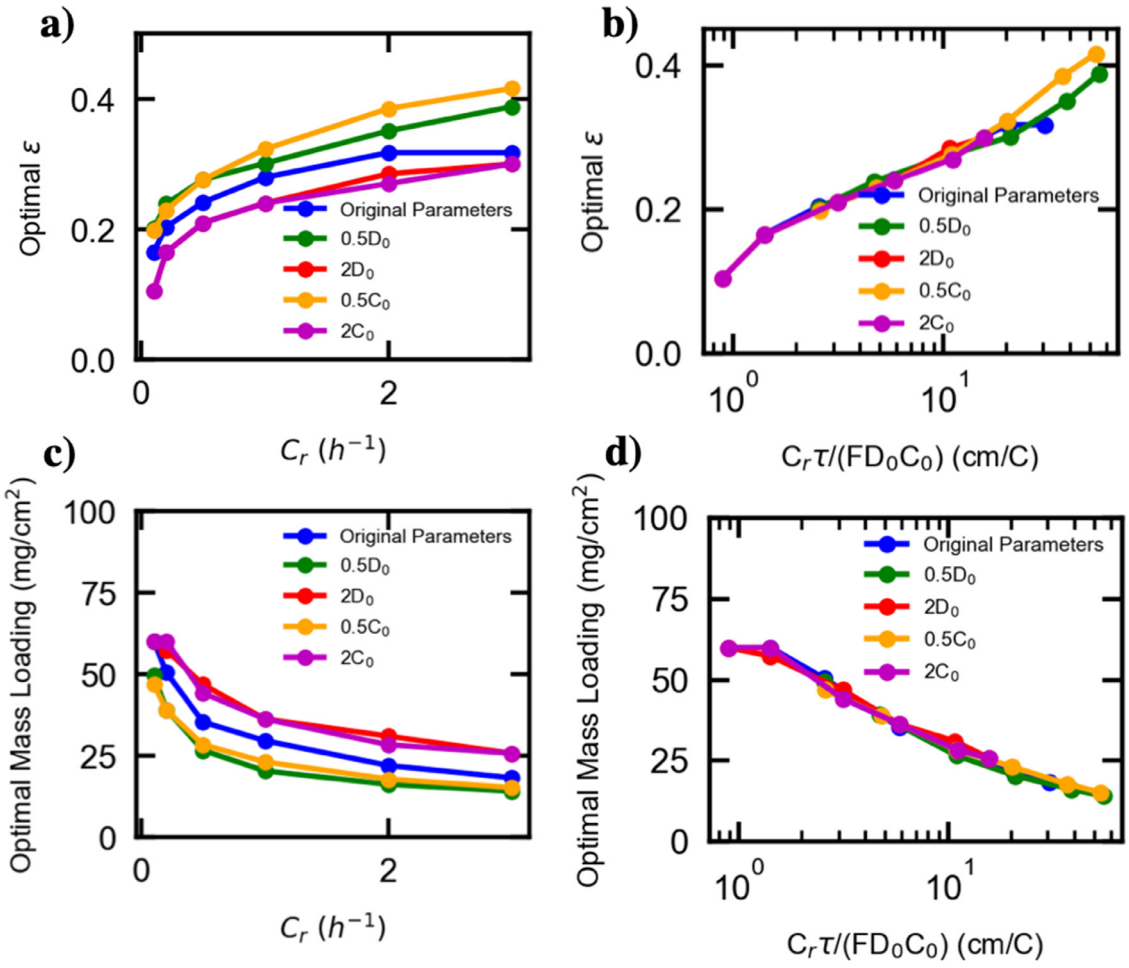

Fig. 5. The optimal electrode parameters depend on electrolyte. For original parameters, $D_0 = 1 \times 10^{-6}$ cm^2 s^{-1}, $c_0 = 1.0$ M, $\tau = \epsilon^{-0.5}$, and results are shown in (a,c) by varying diffusion coefficient or salt concentration. (b,d) When plotted as a function of $C_r\tau/(F D_0 c_0)$, the optimal ϵ and M_A follow a single curve.

scale for Li transport in NMC_{111} electrodes, and thus an agglomerate model most faithfully replicates experiments. Depending on the fabrication processes and the choice of material, the agglomerate size (L_{agg}) and the effective diffusion coefficient (D_{agg}) through the agglomerate may vary. The impact of these parameters on performance is simulated and shown in Fig. 3a, which again shows optimal energy density as a function of C_r. The optimal energy density improves with increasing D_{agg} or decreasing L_{agg}. Changing L_{agg} leads to greater impact on optimal E_V than changing D_{agg} because the time constant for lithium diffusion $\tau_{agg} = \frac{L_{agg}^2}{D_{agg}}$.

3.2. Optimal electrode scale design does not depend on smaller scale parameters

Although the smaller scale ion transport impedance significantly impacts the optimal E_V, it does NOT appear to affect the optimal choices of electrode-scale design parameters. As shown in Fig. 3b and c, although curves with different colors have various agglomerate scale parameters, the optimal ϵ and optimal M_A all overlap, indicating that optimizations with different agglomerate scale properties lead to identical electrode-scale design in order to maximize E_V. Given that electrode-scale design is not affected by smaller scale properties, it is possible to generalize optimization of electrode-scale design parameters, even if each different active material has different smaller scale properties.

3.3. The electrode tortuosity impacts optimum

The electrode tortuosity (τ) may be dependent on multiple parameters, including porosity, active material morphology, as well as the type of conductive filler and binder. Furthermore, the tortuosity may depend on the details of the fabrication processes [28]. Optimization results show that the optimal porosity and mass loading are strongly dependent on tortuosity. However, tortuosity may be difficult to estimate in practice. Commonly, a Bruggeman relationship [29] for spherical particles (Equation 6) is used to estimate the tortuosity as a function the electrode porosity.

$$\tau = \epsilon^{-0.5} \tag{6}$$

However, significant deviations from Equation 6 are often found. For example, an electrode comprised of 2D nanosheets will have higher tortuosity at a given porosity if the sheets stack perpendicular to the diffusion direction [30].

Fig. 4a and c show the optimal porosity and mass loading for assumptions of Bruggeman-like relationships that vary tortuosity by up to a factor of four. Also shown is an extreme case where tortuosity is one for all porosities (black lines). With increasing tortuosity, the effective diffusion coefficient of the electrolyte decreases, and this results in a larger optimal porosity and lower optimal mass loading to retain good electrode utilization. However, if the C-rate (C_r) is multiplied by τ, the optima fall on a single curve, as shown in Fig. 4b and d.

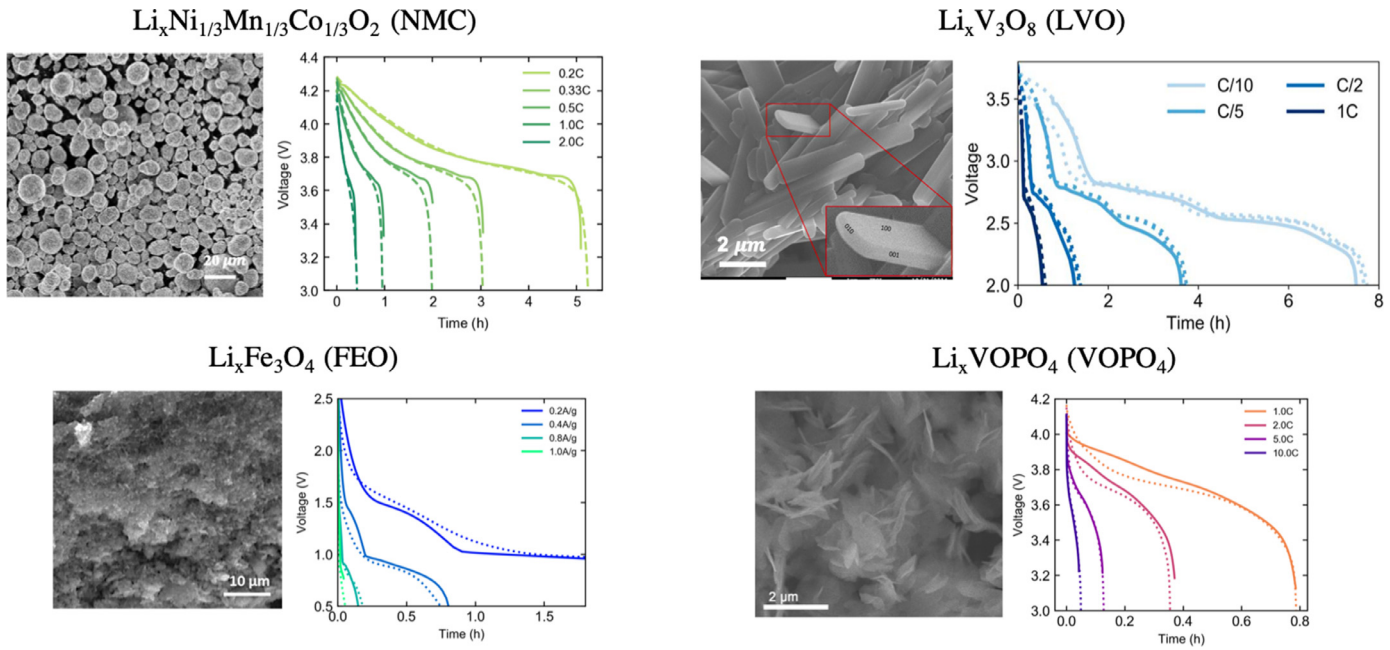

Fig. 6. SEM images of different material [13, 25, 31-33]. Voltage profiles show the agreement between simulations (solid lines) and constant current discharge experiments (dashed lines). The SEM image for LVO are reproduced under terms of the CC BY NC ND License [31]. Copyright 2018, Brady et al., published by ECS. The Voltages profiles for LVO are reproduced under terms of the CC BY License [25]. Copyright 2020, Mayilvahanan et al., published by IOP.

Table 1
Physical properties, tortuosity assumptions and sources of models as well as experiments that models were validated against for different electrodes. The model construction details and experiments to validate model can be found in References column. For FEO, only capacities above 1V were considered. For $VOPO_4$, the model is newly constructed and the detailed information is shown in Supplementary Information.

Active material	Density (g cm^{-3})	Specific Capacity (mAh g^{-1})	Tortuosity assumption	References
NMC	4.6	150	$\tau = \epsilon^{-0.5}$	Hui et al. [13]
LVO	3.15	362	$\tau = \epsilon^{-0.5}$	Mayilvahanan et al. [25]; Brady et al.[31]
FEO	5.15	350	$\tau = \epsilon^{-0.5}$	Zhang et al. [32]; Knehr et al. [34]
$VOPO_4$	2.31	166	$\tau = 14.2\epsilon^{-0.266}$	Ju et al. [33]

3.4. Generalize the difference in electrolyte property

For different materials, the intrinsic electrolyte properties may also vary by changing the Li salt concentration and solvent. Various electrode materials may be paired with different electrolytes due to chemical stability considerations. As shown in Fig. 5a and c, an electrolyte with a lower bulk diffusivity (D_0) or lower salt concentration (c_0) leads to higher optimal porosity and lower optimal mass loading. We found the optima overlap if the C_r is multiplied by $\frac{1}{FD_0c_0}$, as shown in Fig. 5b and d. Such results indicate that it is possible to generalize optimal design rules to systems with different electrolytes. For example, consider two electrode systems using electrolytes with different diffusivity ($D_0 = 1 \times 10^{-6}$ cm^2 s^{-1} vs 2×10^{-6} cm^2 s^{-1}). As shown in Fig. 5a and c, electrodes with lower D_0 (blue curves) have higher optimal porosity and lower optimal mass loading. Such impact on optimal designs is generalized in Fig. 5b and d by rescaling the x-axis to account for the different electrolyte properties.

In summary, after rescaling C_r with $\frac{\tau}{FD_0c_0}$, the effect of variations in electrode tortuosity and electrolyte properties can be accounted for with a single curve for the case of NMC. The underlying physical explanation of such rescaling is discussed in the next section. With the findings that electrode-scale optimal design is independent of the smaller scale properties and the impact of different electrode-scale parameters can be generalized, we extended the material-specific optimal electrode design rule to make it more generally applicable.

4. Discussion

4.1. Smaller scale structures and physics-based models of different electrodes

Fig. 6 shows four distinct electrode materials that have been modeled and experimentally validated. Table 1 provides the sources of model construction and parameters. As seen in the SEM micrographs, NMC and FEO have nanometer-sized crystals that agglomerate into secondary particles (agglomerates), while the smaller-scale ion transport impedance for LVO and $VOPO_4$ is dominated by the crystal scale with lateral size of microns. Such structural differences lead to varying small-scale ion transport impedances. Moreover, LVO and FEO undergo a reversible phase change during lithiation and de-lithiation, shown by the voltage plateaus on discharge voltage profiles.

Following the procedure outlined for optimization of NMC electrodes in the previous section, optimization of electrode-scale design of each of these cathode materials was conducted using previously validated physics-based models [13, 25, 34], for which agreement with experiments are shown in Fig. 6. The P2D models have significantly different physics on the smaller scale, but electrode-scale formulations

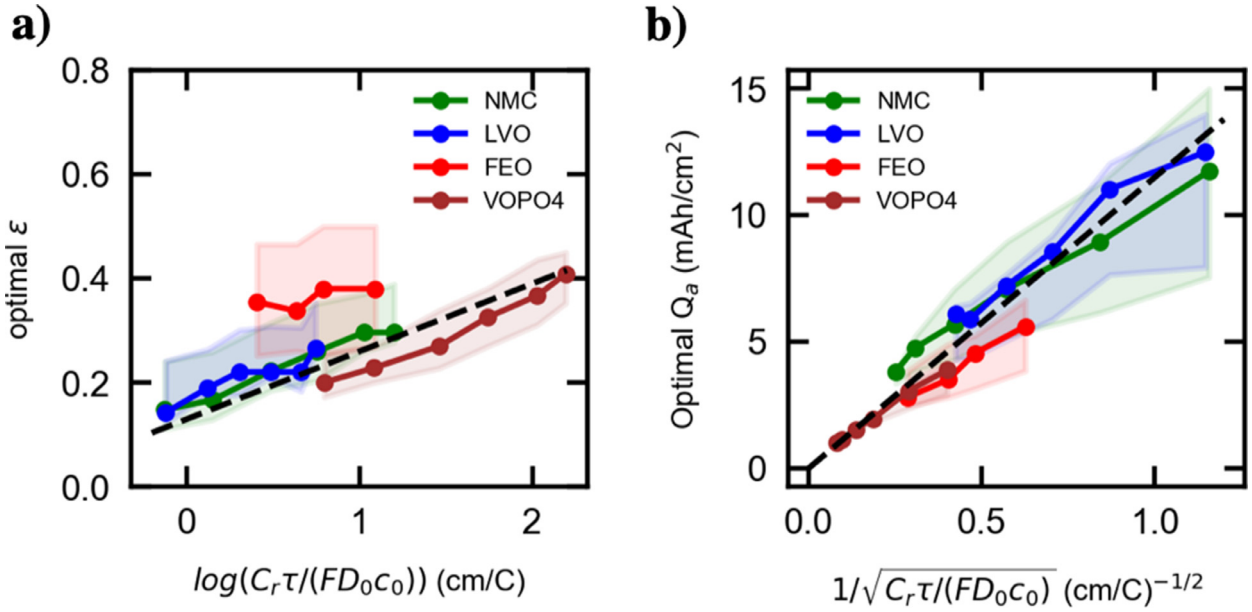

Fig. 7. Optimal design results for 4 different materials, plotted vs rescaled current rate. Assumptions: $D_0 = 1 \times 10^{-6}$ cm^2 s^{-1}, $c_0 = 1.0$ M for all electrodes. Optimal ϵ and Q_a are shown by solid lines. Shaded regions indicate sensitivity of the parameter values by showing region to achieve 95% of the maximum E_V. Black dashed lines indicate the general correlation between rescaled C_r and optimal designs.

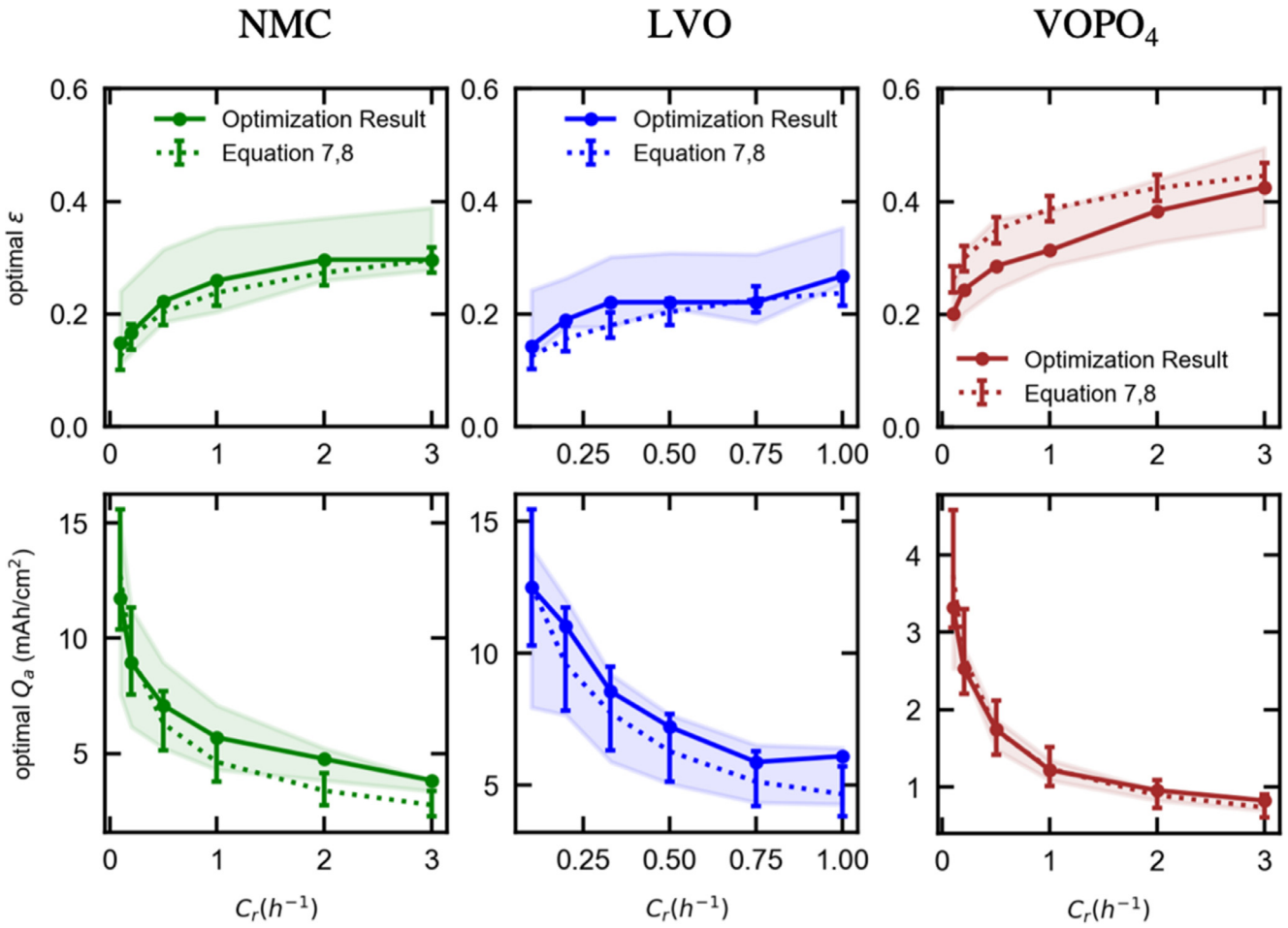

Fig. 8. Simulated optimal design results and correlation predictions as a function of C_r. Solid lines show numerical optimization results, and the shaded regions indicate parameter values to achieve 95% of maximum E_V. The dashed lines are calculated using Equation 7 and 8, combined with material specific properties. Error bars describe the optimization results with an assumption of ± 50 % uncertainty in tortuosity.

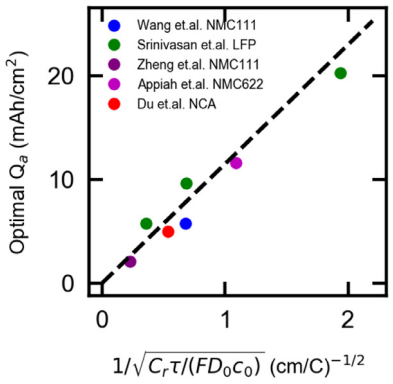

Fig. 9. Compare general design results on optimal Q_a (same black dashed line in Fig. 7b) with optimization results on specific material from others' study. Legend shows the source of study and the type of active material been optimized.

are identical. Table 1 lists key material properties and sources of model & experimental data for the four active materials studied in this work. Detailed descriptions of the models describing the smaller-scale physics for each of these models can be found in the references provided in Table 1, or in the Supplementary Information for $VOPO_4$.

4.2. Summary for different electrodes

Fig. 7 shows the optimization results of cells with different materials as the cathode, assuming graphite as an anode with an n/p capacity ratio (ratio between graphite electrode capacity and positive electrode capacity) of 1 and with a fixed anode porosity of 0.35. Again, it is assumed that $V_{AM}/(V_{AM}+V_{inert}) = 0.9$. As shown in Fig. S4, varying the volume fraction of inert additives (C_{65} and PVDF) impacts optimal design in a generalizable manner.

In Fig. 7b, the loadings of active material are given as capacity loading Q_a ($= \frac{M_A Q_{cathode}}{10^3}$). The solid lines in Fig. 7a, b present the optimal design parameters to achieve highest E_V, while the shaded regions give sensitivity, indicating a range that allows for achievement of 95% of the maximum E_V. The optimal Q_a results on Fig. 7b follow a (dashed) trend line. The optimal porosity ε is in Fig. 7a. Despite the outlier FEO (with analysis in Supplementary Information, Fig. S2), the optimal ε of all other materials overlap, especially accounting for the 95% sensitivity contours. This suggests a generalized optimal design rule, which is independent of the active material.

Moreover, Fig. S3 shows the effect of changing anode material or changing capacity ratio. The comparison indicates that the generalized optimal design rule on the cathode is not affected by the choice of anode materials or cathode/anode capacity ratios.

4.3. Generalized Optimal Design Rule

As shown by the black dashed lines on Fig. 7, two relations describing the relation between general design optimal parameters and generalized C_r were obtained:

$$\epsilon = 0.13 \log_{10}\left(k_\epsilon \frac{C_r \tau}{F D_0 c_0} \right) \tag{7}$$

$$Q_a = k_Q / \sqrt{k_\epsilon C_r \tau / (F D_0 c_0)} \tag{8}$$

where the constants k_ε = 11.94 C cm^{-1} and k_Q = 38.03 mAh cm^{-2}. Since electrode tortuosity τ is anticipated to be dependent on porosity (Bruggeman relation for spherical particles for example), one may need to solve Equation 7 and the known $\tau = f(\epsilon)$ relation simultaneously to obtain optimal ϵ, and then to use Equation 8 to estimate the optimal areal capacity loading Q_a. Fig. 8 shows the results of optimal ε and Q_a calculated using Equations 7 and 8 (dashed lines), which agree well with numerical optimization results (solid lines), especially with the 95% sensitivity contours (shaded regions in Fig. 7).

As a means of understanding Equations 7 and 8, a dimensional analysis on a representative model [13] was conducted, and the dimensionless capacity is given by

$$\overline{Q_a} = \frac{C_r Q_a L_{cathode} \tau}{D_0 c_0 F \epsilon} \tag{9}$$

where $L_{cathode}$ can be replaced using Equation 3,

$$\overline{Q_a} = \frac{C_r \tau Q_a^2}{V_{AM} D_0 c_0 F Q_{cathode} \rho_M \epsilon} \tag{10}$$

Physically, $\overline{Q_a}$ can also be understood as an applied current density normalized by a limiting current density. Rearranging Equation 10 suggests the correlation 8, in which Q_a is inversely proportional to $\sqrt{k_\epsilon C_r \tau/(F D_0 c_0)}$.

The practical use of equations 7 and 8 may be problematic when the porosity-tortuosity relation is not known with certainty. We explored through simulations how a poorly characterized tortuosity may create uncertainty in the optimal porosity and loading. In Fig. 8, the

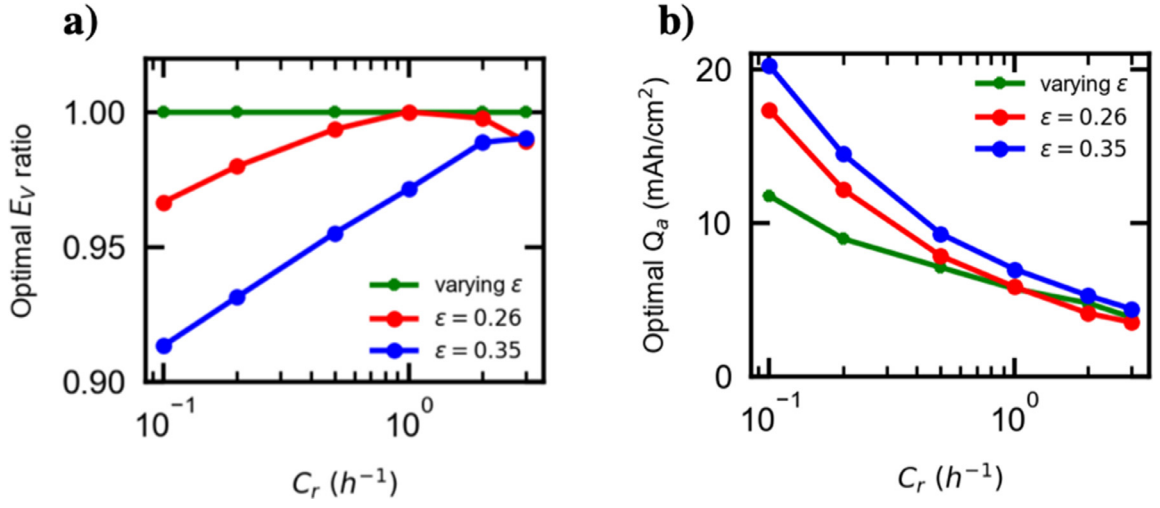

Fig. 10. (a) (Optimal cell E_V assuming ε is constant) / (Optimal cell E_V assuming ε is free to vary). (b) Optimal capacity loading under different ε assumptions.

uncertainty in the optimal design parameters assuming a 50% uncertainty in τ are represented by error bars. The results are overlaid on the optima as determined by the physics-based modeling results, on which the correlation was trained. In most cases, the resulting range of recommendations from the correlation lie still within 95% of the maximum achievable E_V, designated by the shaded regions in Fig. 8.

Fig. 9 shows the comparison between Equation 8 and optimization results on specific electrode reported by others [18,19, 35–37]. Equation 8 suggests optimal Q_a that is close to previously reported results, even for optima derived with slightly different constraints. Also, the correlation seems to apply also to NCA, NMC_{622}, and LFP, not studied directly in the development of the present correlation.

4.4. Assuming limitation on low porosity

According to Fig. 7a, the optimal porosities for cells at low C_r are less than 0.2, which may be hard to reach due to practical limitations. For instance, for close packed solid spherical particles, the lowest porosity is 0.26. Thus, at the lower C_r, the low, optimal porosities may not be readily achievable. Therefore, Fig. 10 shows the optimization results obtained if the porosity is assumed to be fixed. In Fig. 10a, the optimal cell E_V for a fixed porosity of 0.26 and 0.35 (assumed to be the practical value by calendering) is normalized by the value obtained by varying both porosity and loading, as in Fig. 2. It is seen that the loss in performance is minimal at high C_r, and is less than 10 % at low C_r. Fig. 10b shows that the optimal capacity loading deviates significantly from the results in Fig. 2 (reproduced as the red line) at low C_r. However, as suggested in Fig. 2, the optimal cell E_V is relatively insensitive to porosity and loading at low C_r. Practically, setting Q_a = 20.21 mAh cm^{-2} at C/10 when fixing porosity at 0.35 instead of using Q_a = 11.74 mAh cm^{-2} for freely varying ε, diminishes E_V only by 8.68 %. In summary, this section provides a sensitivity analysis on the electrode porosity to connect the optimal design with practical applications. Under practical conditions, it might be hard to calender thick electrodes towards extremely low ε. The result on Fig. 10 shows that the limitations on electrode porosity mainly impact the design for low-rate battery (C_r < 1.0 h^{-1}), and the reduction in optimal cell E_V is relatively small, within 10%.

5. Conclusions

Batteries are complex, multi-scale systems, and ion transport impedances on different scales affect performance. With experimentally validated multiscale physics-based models, this work reveals that the optimization of battery's electrode-scale ion transport is not affected by the material properties on the smaller scales. Taking into account the salt diffusivity, salt concentration and electrode tortuosity, generalized electrode-scale optimization is applied to multiple electrodes, obtaining simple correlations. Results show that the tortuosity is important to optimal design, but optimizations can be performed with reasonable certainty when the tortuosity estimation is in error by 50%. Correlations obtained in the present investigation can provide a generalized guide for optimal design of other battery electrode materials, as shown by comparison with the literature.

Declaration of Competing Interest

The authors declare that they have no known competing financial interests or personal relationships that could have appeared to influence the work reported in this paper.

CRediT authorship contribution statement

Zeyu Hui: Conceptualization, Methodology, Software, Writing – original draft. **Karthik S. Mayilvahanan:** Software, Validation, Visualization. **Krystian Ganko:** Software. **Yuan Yang:** Resources, Writing – review & editing. **Xiao Zhang:** Resources, Validation. **Zhengyu Ju:** Resources, Validation. **Kenneth J. Takeuchi:** Supervision. **Amy C. Marschilok:** Resources, Supervision. **Guihua Yu:** Resources, Writing – review & editing, Supervision. **Esther Takeuchi:** Project administration, Funding acquisition, Supervision. **Alan C. West:** Conceptualization, Writing – review & editing, Funding acquisition, Supervision.

Acknowledgement & Funding Sources

This research was supported as part of the Center for Mesoscale Transport Properties, an Energy Frontier Research Center supported by the U.S. Department of Energy, Office of Science, Basic Energy Sciences, under award #DE-SC0012673 for financial support. EST acknowledges the William and Jane Knapp Chair of Energy and the Environment.

Supplementary materials

Supplementary material associated with this article can be found, in the online version, at doi:10.1016/j.ensm.2021.04.018.

References

[1] J.P. Barton, D.G. Infield, IEEE Transactions on Energy Conversion 19 (2004) 441–448.
[2] K.C. Divya, J. Østergaard, Electric Power Systems Research 79 (2009) 511–520.
[3] I. Hadjipaschalis, A. Poullikkas, V. Efthimiou, Renewable and Sustainable Energy Reviews 13 (2009) 1513–1522.
[4] J.M. Tarascon, M. Armand, in: Materials for Sustainable Energy, Co-Published with Macmillan Publishers Ltd, UK, 2010, pp. 171–179.
[5] https://www.energy.gov/sites/prod/files/2016/06/f32/es000_howell_2016_o_web.pdf.
[6] G. Berckmans, M. Messagie, J. Smekens, N. Omar, L. Vanhaverbeke, J. Van Mierlo, Energies 10 (2017).
[7] R. Marom, S.F. Amalraj, N. Leifer, D. Jacob, D. Aurbach, Journal of Materials Chemistry 21 (2011) 9938–9954.
[8] V. Etacheri, R. Marom, R. Elazari, G. Salitra, D. Aurbach, Energy & Environmental Science 4 (2011) 3243–3262.
[9] A. Manthiram, X. Yu, S. Wang, Nature Reviews Materials 2 (2017) 16103.
[10] L.O. ValøEn, J.N. Reimers, Journal of The Electrochemical Society 152 (2005) A882.
[11] C. Yu, S. Ganapathy, E.R.H.V. Eck, H. Wang, S. Basak, Z. Li, M. Wagemaker, Nature Communications 8 (2017) 1086.
[12] M.D. Radin, S. Hy, M. Sina, C. Fang, H. Liu, J. Vinckeviciute, M. Zhang, M.S. Whittingham, Y.S. Meng, A. Van Der Ven, Advanced Energy Materials 7 (2017) 1602888.
[13] Z. Hui, K.S. Mayilvahanan, Y. Yang, A.C. West, Journal of The Electrochemical Society 167 (2020) 100542.
[14] H. Zhang, X. Yu, P.V. Braun, Nature Nanotechnology 6 (2011) 277–281.
[15] N. Li, Z. Chen, W. Ren, F. Li, H.-M. Cheng, Proceedings of the National Academy of Sciences 109 (2012) 17360.
[16] T.F. Fuller, M. Doyle, J. Newman, Journal of The Electrochemical Society 141 (1994) 1–10.
[17] J. Newman, Journal of The Electrochemical Society 142 (1995) 97–101.
[18] V. Srinivasan, J. Newman, Journal of the Electrochemical Society 151 (2004) A1517–A1529.
[19] W.A. Appiah, J. Park, S. Song, S. Byun, M.-H. Ryou, Y.M. Lee, Journal of Power Sources 319 (2016) 147–158.
[20] S. De, P.W.C. Northrop, V. Ramadesigan, V.R. Subramanian, Journal of Power Sources 227 (2013) 161–170.
[21] Https://Cuit.Columbia.Edu/Shared-Research-Computing-Facility.
[22] M. Doyle, T.F. Fuller, J. Newman, Journal of The Electrochemical Society 140 (1993) 1526–1533.
[23] B. Paxton, J. Newman, Journal of The Electrochemical Society 144 (1997) 3818–3831.
[24] Y. Kuang, C. Chen, D. Kirsch, L. Hu, Advanced Energy Materials 9 (2019) 1901457.
[25] K. Mayilvahanan, N. Brady, A.H. Mccarthy, L. Wang, A.C. Marschilok, K. Takeuchi, E. Takeuchi, A.C. West, Journal of The Electrochemical Society 167 (2020) 100503.
[26] Z. Ju, X. Zhang, S.T. King, C.D. Quilty, Y. Zhu, K.J. Takeuchi, E.S. Takeuchi, D.C. Bock, L. Wang, A.C. Marschilok, G. Yu, Applied Physics Reviews 7 (2020) 041405.
[27] G. Cunningham, M. Lotya, N. Mcevoy, G.S. Duesberg, P. Van Der Schoot, J.N. Coleman, Nanoscale 4 (2012) 6260–6264.
[28] R. Morasch, J. Landesfeind, B. Suthar, H.A. Gasteiger, Journal of The Electrochemical Society 165 (2018) A3459–A3467.
[29] D.a.G. Bruggeman, Annalen der Physik 416 (1935) 636–664.
[30] J. Landesfeind, J. Hattendorff, A. Ehrl, W.A. Wall, H.A. Gasteiger, Journal of The Electrochemical Society 163 (2016) A1373–A1387.
[31] N.W. Brady, Q. Zhang, K.W. Knehr, P. Liu, A.C. Marschilok, K.J. Takeuchi, E.S. Takeuchi, A.C. West, Journal of The Electrochemical Society 163 (2016) A2890–A2898.

[32] X. Zhang, Z. Ju, L.M. Housel, L. Wang, Y. Zhu, G. Singh, N. Sadique, K.J. Takeuchi, E.S. Takeuchi, A.C. Marschilok, G. Yu, Nano Letters 19 (2019) 8255–8261.
[33] Z. Ju, Y. Zhu, X. Zhang, D.M. Lutz, Z. Fang, K.J. Takeuchi, E.S. Takeuchi, A.C. Marschilok, G. Yu, Chem Mater 32 (2020) 1684–1692.
[34] K.W. Knehr, N.W. Brady, C.A. Cama, D.C. Bock, Z. Lin, C.N. Lininger, A.C. Marschilok, K.J. Takeuchi, E.S. Takeuchi, A.C. West, Journal of the Electrochemical Society 162 (2015) A2817–A2826.
[35] F. Wang, M. Tang, Cell Reports Physical Science 1 (2020) 100192.
[36] H. Zheng, J. Li, X. Song, G. Liu, V.S. Battaglia, Electrochimica Acta 71 (2012) 258–265.
[37] Z.J. Du, D. Wood, C. Daniel, S. Kalnaus, J.L. Li, J Appl Electrochem 47 (2017) 405–415.